

PAPER

Water-based resistive switches for neuromorphic long-range connections

To cite this article: Akshay Ananthakrishnan *et al* 2021 *J. Phys. D: Appl. Phys.* **54** 225104

View the [article online](#) for updates and enhancements.



IOP | ebooks™

Bringing together innovative digital publishing with leading authors from the global scientific community.

Start exploring the collection—download the first chapter of every title for free.

Water-based resistive switches for neuromorphic long-range connections

Akshay Ananthakrishnan^{1,*} , Xingyu Du¹ and Mark G Allen^{1,2} 

¹ Department of Mechanical Engineering and Applied Mechanics, University of Pennsylvania, Philadelphia, PA, United States of America

² Department of Electrical and Systems Engineering, University of Pennsylvania, Philadelphia, PA, United States of America

E-mail: akshayan@seas.upenn.edu

Received 14 June 2020, revised 20 February 2021

Accepted for publication 1 March 2021

Published 15 March 2021



CrossMark

Abstract

The brain's small-world network utilizes its short-range and long-range synaptic connections to process information in a complex and energy-efficient manner. To emulate the former, neuromorphic hardware typically leverages the conductance switching properties of thin-film dielectrics and semiconductors. Because these materials offer low ion mobilities, long-range connections built from thicker dielectrics require impractically-large forming voltages. To overcome this intrinsic shortcoming of solid-state active media, we present in this paper a simple Ag–H₂O–Au cell that takes advantage of the relatively high ion mobility offered by deionized water to enable programmable connectivity switches between neurons separated by large gaps ($\sim 40 \mu\text{m}$). We introduce dual voltage programming schemes that allow the switch conductance to be modulated in analog and digital steps. When operating in the analog mode, the switch conductance could be potentiated and depressed over a relatively large ($3.5\times$) range. In the digital mode, the Ag–H₂O–Au switch delivered a high ON/OFF current ratio of ~ 600 and sustained this margin over 200 switching cycles. Additionally, both switch states could be maintained for at least 3 h without external power. We show that unlike their solid-state counterparts, the water-gap in the Ag–H₂O–Au cell can be easily refreshed without compromising the switching functionality. These attributes of Ag–H₂O–Au switches in addition to their biocompatibility and simple design make them attractive for neuromorphic wetware implementations.

Supplementary material for this article is available [online](#)

Keywords: resistive switch, liquid synapse, long-range connection, neuromorphic, silver dendrite, electrochemical

(Some figures may appear in colour only in the online journal)

1. Introduction

Human brain graphs constructed from functional magnetic resonance imaging and diffusion tensor imaging display small-world connectivity [1–4]. Brain networks employ dense short-range (SR) synaptic connections to realize functional modules at local scales, and sparse intermodular long-range (LR) connections to integrate information at the global scale

[5]. This connectivity pattern allows the brain to lower the wiring cost associated with LR connections without compromising the adaptability and functional complexity enabled by SR connections [6]. In addition to enhancing global efficiency, LR connections also co-ordinate brain-wide spatiotemporal activities [7, 8] and they play key roles in endowing humans with general intelligence [5] and preventing brain disorders [9]. Their importance is concretized by the unexpectedly large fraction of long-range axonal projections found in the cat primary visual cortex [10]. The length of inter-areal axonal

* Author to whom any correspondence should be addressed.

projections depends on several factors, including but not limited to the brain regions they serve; many studies estimate them at 1–50 mm [11–13].

The brain's remarkable cognitive processing capabilities and physical makeup inspired the idea of neuromorphic computers [14, 15]. These specialized computing units generally adopt a feedforward network architecture comprising layers of electrical neurons interconnected via SR resistive switches. Due to their metal/insulator/metal construction, two-terminal memristors are placed at the crosspoints of overlapping wires, allowing the inter-wire conductances to be programmed in analog (full weight precision) or digital (binary weights) steps [16–20]. Accordingly, a network of SR synapses is compactly emulated using a crossbar array of SR resistive switches. This hardware representation not only supports the density requirements of SR synapses but also faithfully implements the weighted-sum synaptic operations [21–26]. In comparison to hardware designs utilizing transistor-based switches, those employing resistive switches typically report higher speed, power-efficiency, and circuit densities [27–30]. The physical mechanisms responsible for resistive switching are relatively simple and have been realized in a variety of material systems, including binary and ternary metal-oxides as well as organic materials [14, 31]. However, despite these advantages, limited progress has been achieved in realizing LR connections using resistive switches. This can be attributed to two reasons: (a) software—the lack of algorithms that fully leverage LR connections for performance gains and (b) hardware—implementing long-range connections with solid-state resistive switches requires impractically large ‘forming’ voltages as discussed below.

To be configured for operation, an as-fabricated resistive switch typically undergoes a ‘forming’ process, where its dielectric layer (a few tens to a few hundreds of nanometers thick) is subjected to breakdown-inducing potentials of \sim few volts [22, 32–34]. Once formed, these devices can be repeatedly switched between high (HRS) and low (LRS) resistance states in analog or digital steps [21]. Although this approach works well for thin-film SR switches, the linear scaling of forming voltage with dielectric thickness [32, 35] impedes the construction of LR switches from thicker active layers. Compared with solid-state dielectrics, liquid media offer higher ion mobilities and will therefore require substantially lower forming voltages for implementing LR switches. Due to its biocompatibility, solvation properties, and amenability to small-world network formation, water is an exciting candidate for LR switches. Its neuromorphic chemistry could help find interesting applications in ad-hoc pattern recognition circuits for closed-loop bioelectronic devices [36].

Previous research has already demonstrated the transistor-gating properties of liquid electrolytes [36, 37]. Here, device conductances were controlled either via charging of the Debye-Helmholtz layer or through bulk injection of ions into the channel [36]. However, like their solid-state analogs, the widespread adoption of three-terminal electrolyte-gated transistors has been challenged by emerging quasi-liquid [38] and liquid-based [39–43] two-terminal resistive switches. Guo *et al* were among the first to demonstrate reversible growth

and erasure of Ag filaments in an Ag–H₂O–Pt electrochemical cell [39]. However, as this study was primarily focused on uncovering the physical mechanisms responsible for resistive switching in Ag-based devices, it did not characterize the cell with regards to its analog operability, endurance, and non-volatility. Also, all experiments were performed in a 2D cell that likely favored the formation of substrate-hugging rather than freely suspended Ag filaments. Thus, the controlled growth and erasure of unsupported high aspect ratio filaments, a demonstration that is relevant to crossbar geometries, remained unaddressed. Nonetheless, this proof of concept study was important as it laid the foundations for further inquiries into liquid-based resistive switches. For instance, Han *et al* built resistive switches from CuSO₄-filled nanoporous polycarbonate membranes (6 μ m thickness) and demonstrated acceptable endurance characteristics [43]. However, this work did not characterize the non-volatility and analog switching properties of the electrochemical cell; it also reported substantial performance degradations in thicker membranes. Given these shortcomings, the recent study by Kim and Lee, which demonstrated low-voltage analog and digital switching in low concentrations (0.05 M) of AgNO₃ solution, deserves special mention [40]. However, all experiments were performed using a highly asymmetric electrode configuration comprising of a flat Ag electrode and an inert probe tip. Hence, it is reasonable to expect that the large tip curvature encouraged the formation of thinner Ag filaments (compared with crossbar geometries) by elevating the local electric field density [44]. Despite the inherent reset bias of this electrode configuration, the AgNO₃ - based switch endured only 100 switching cycles and provided a relatively low ON/OFF current ratio of \sim 5. Also, the LRS and HRS could be retained over a very short duration of \sim 15 min.

Apart from the electrochemical metallization approaches discussed so far, where aqueous switching is mediated by the growth and erasure of bridging metal deposits, some studies have also exploited the resistance switching properties of semiconductor–electrolyte interfaces. For instance, Sun *et al* showed how voltage-controlled oxidation and de-oxidation of silicon–electrolyte interfaces could be used to build fluid-based digital memories and latching circuits [41]. In another study, Hassan *et al* took advantage of Schottky barriers formed at the ITO–ZnO interface of the ITO–ZnO–H₂O–Ag cell and the selective transport of OH[−] ions in ZnO to achieve digital switching. To produce the required concentration of H⁺ and OH[−] ions, water was electrolyzed at sufficiently high voltages [42]. However, both studies discussed above utilized non-crossbar geometries and did not provide evidence of the retention and gradual conductance switching properties. Notably, because these works relied on interfacial switching, maintaining a stable LRS demanded high concentrations of supporting electrolytes [41] and/or higher than usual programming voltages [42]. These requirements do not favor the development of power-efficient and biocompatible LR switches.

The device implementations discussed above highlight the need for a crossbar-compatible two-terminal resistive switch that can harness the advantages of electrochemical

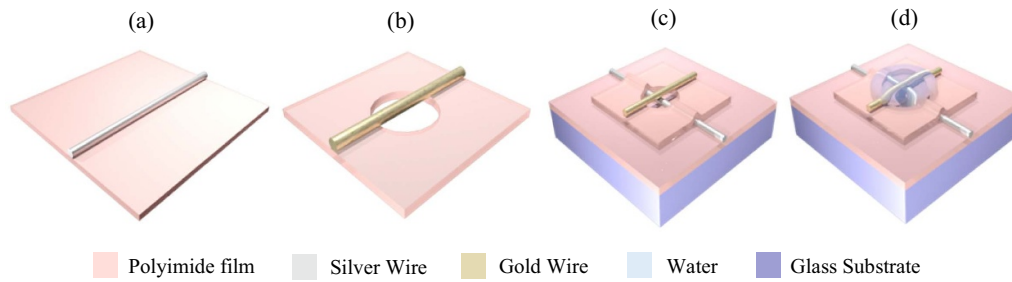


Figure 1. Fabrication of the Ag–H₂O–Au LR switch (a) adhering a 70 μm silver wire onto a polyimide film; (b) adhering a 50 μm gold wire onto a polyimide film; (c) orthogonal stacking of Ag (bottom) and Au (top) wires, and (d) injecting a water droplet at the cross-point gap separating the Au and Ag wires.

metallization to implement programmable LR connections. To address this, we present in this paper, a water-based non-volatile LR switch whose conductance can be tuned in analog and digital steps within a reasonably large resistance window, while maintaining relatively high ON/OFF current margins. This switch is constructed from an Ag–H₂O–Au electrochemical cell where the Ag and Au wires are separated by a large gap ($\sim 40 \mu\text{m}$) filled with deionized water. By optically interrogating the cell in real-time, we identify the physical mechanisms underlying its conductance switching properties. The highlights of this device are its simplistic design, biocompatible construction, low-voltage operation, and high ON–OFF current margin. Having described the motivation for this work, the next section outlines the steps involved in the fabrication of the Ag–H₂O–Au LR switch. The third section describes its performance attributes namely, its gradual conductance response to low-voltage excitations, endurance, and non-volatility. These are compared to prior demonstrations of liquid-based switches to position the findings of this study in the appropriate context. The conclusion section showcases the key takeaways of this work.

2. Fabrication

Figure 1 illustrates the straightforward fabrication of the Ag–H₂O–Au LR switch. Firstly, as shown in figures 1(a) and (b), solid Ag (diameter = 76 μm) and Au (diameter = 51 μm) wires were stretched taut and laid onto the adhesive sides of two separate 25 μm thick polyimide films. As shown in (b), the Au wire was suspended over a laser-patterned central hole in the top polyimide film. Cross-stacking the two films (keeping the Au wire on top) produced a well-like structure with the Ag–Au crosspoint positioned squarely inside it (see figure 1(c)). Injecting a water droplet into this depression yielded the desired Ag (bottom)–H₂O (gap)–Au (top) switch configuration. To estimate the as-fabricated interelectrode gap, the well-like structure in one of the representative samples was filled with polydimethylsiloxane (PDMS) instead of water. The entire structure was then locked in place by thermally curing the PDMS elastomer. Subsequently, the Ag–PDMS–Au stack was vertically sectioned near the cross-point (see figure 2(a)) and placed under the microscope (cross-section facing toward the objective) for optical analysis. As shown in figure 2(b), the measured gaps were about 40 μm , at least

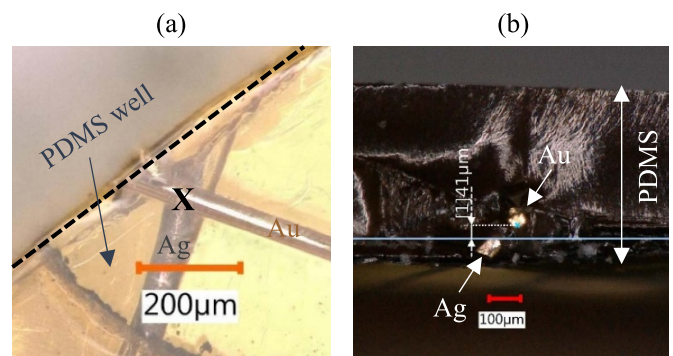


Figure 2. Measurement of the Ag–Au interwire gap using a moulded Ag–PDMS (gap)–Au construct. (a) Top view of the moulded structure. The dotted line identifies the vertical slice next to the cross-point (marked ‘X’); (b) cross-sectional view of the Ag–PDMS–Au crossbar showing the $\sim 40 \mu\text{m}$ PDMS gap.

two to three orders of magnitude larger than the thicknesses of conventional solid-state switching media used in SR switches e.g. 5 nm TaO_x in [18], 8 nm NbO₂ in [19], and 20 nm HfO_{2–x} in [34].

3. Experiments

The use of pure deionized water i.e. without any supporting electrolytes meant that the as-fabricated Ag–H₂O–Au LR switch manifested an ‘open’ state (see figure 3(a)). To achieve switch operation, it was first necessary to ‘form’ the device by growing a mechanically stable and electrically conductive Ag link across the water gap (see figure 3(b)). This could be achieved by anodically biasing the Ag electrode at potentials $\geq 1.5 \text{ V}$. Figures 3(c) and (d) show how applying a 2 V DC bias to the Ag electrode of a representative synapse dramatically reduced the water-gap resistance. Here, the filament’s conductance was limited to 0.0011 S by enforcing a compliance current $I_{\text{cc}} = 2 \text{ mA}$. Simultaneous optical interrogation helped uncover the mechanism of filament formation. When subjected to anodic potentials, the Ag wire produced water-soluble Ag⁺ ions via a silver oxide intermediate. Under the influence of sufficiently high electric fields, these ions drifted across the large water gap (thanks to the high ionic mobility of water) to the Au wire, where they were reduced to metallic Ag. Since the entire electrodeposition process

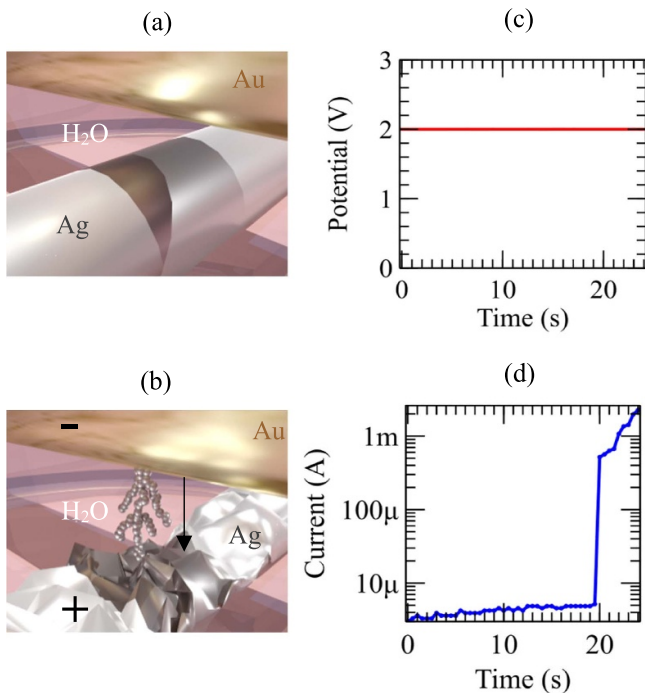


Figure 3. Electrical ‘forming’ of the Ag–H₂O–Au LR switch (a) the as-fabricated device in ‘open’ state due to the insulating water-gap; (b) the ‘formed’ switch in a low resistance state due to the presence of a bridging Ag link; (c) forming voltage applied to the Ag anode, and (d) current response of the Ag–H₂O–Au switch during the forming process. Note that the Ag link grows from the Au electrode toward the Ag electrode and the sudden ramp in current at ~ 20 s signifies a contact between the growing Ag link and the Ag electrode.

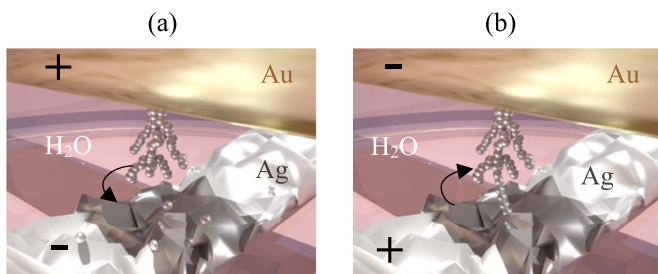


Figure 4. Low-voltage programmability of the Ag–H₂O–Au LR switch (a) the -0.2 V/1 s reset pulses dissolve the highly resistive portions of the Ag filament, thereby creating a small gap and (b) the $+0.2$ V/1 s set pulses re-grow Ag bridges across the small gap created by the previous reset process in (a).

was transport-limited, the resulting Ag filaments assumed a dendritic morphology as they grew from the Au cathode to the Ag anode. The forming process was deemed complete when the Ag dendrite developed a sufficiently strong contact (determined by I_{cc}) with the Ag wire anode. Once formed, the Ag–H₂O–Au LR switch required much lower potentials to switch between its non-volatile LRS and HRS. This could be attributed to the growth and dissolution of the highly resistive portions of the ‘formed’ Ag link [45, 46]. Figures 4(a) and (b) describe this mechanism schematically (see supplementary videos for the real-time demonstration, available online at stacks.iop.org/JPD/54/225104/mmedia).

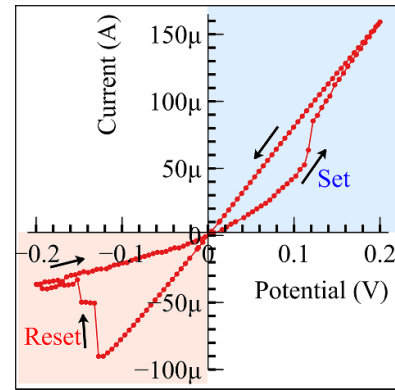


Figure 5. A cyclic voltammogram of the Ag–H₂O–Au LR switch characterizing its hysteretic I – V response. Here the current was measured in response to a 0 V \rightarrow 0.2 V \rightarrow -0.2 V \rightarrow 0 V DC voltage sweep. The arrows indicate the sweep direction where the first quadrant describes the HRS \rightarrow LRS set process, and the third quadrant portrays the LRS \rightarrow HRS reset process.

To record its hysteretic fingerprint, the synapse was subjected to the following DC voltage sweep: 0 V \rightarrow 0.2 V \rightarrow -0.2 V \rightarrow 0 V. Starting from an initial HRS, the 0 V \rightarrow 0.2 V ramp transformed the Ag–H₂O–Au switch to its LRS (see the increase in operating current in the first quadrant of figure 5). Thereafter, the switch retained the LRS during the subsequent 0.2 V \rightarrow -0.2 V deramp, until the applied potential reached -0.1 V. At this point, the resistive portions of the Ag link dissolved, lowering the synapse’s conductance and ‘resetting’ it back to HRS (see figure 4(a)). The switch maintained this HRS during the final -0.2 V \rightarrow 0 V ramp. Based on the observed linearity of the I – V segments between ± 80 mV and ± 80 mV, a read pulse amplitude of 50 mV was utilized for evaluating switch states throughout this paper.

The adaptability and learnability of biological neural networks stem from their ability to fine-tune their SR and LR synaptic strengths. Figures 6(a) and (b) highlight similar analog switching, i.e. long-term potentiation (LTP) and long-term depression (LTD) capabilities of the Ag–H₂O–Au LR switch. The results in figure 6(a) were obtained using short ± 0.2 V set and reset pulses (pulse width = 0.2 s) whereas those in figure 6(b) utilized relatively longer ± 0.2 V set and reset pulses (pulse width = 0.4 s). These observations showcase the expected trade-off between conductance resolution and programming times. Irrespective of the pulse width employed, the switch conductances could be tuned across a relatively wide resistance range (normalized) of ~ 3.5 .

Maintaining a long and thin filamentary backbone in a highly diffusive medium, such as water, challenges the endurance of LR switches. Hence, to evaluate its cyclability, the Ag–H₂O–Au cell was switched between its LRS and HRS via repeated (and alternative) application of $+0.2$ V/1 s set (HRS \rightarrow LRS) and -0.2 V/1 s reset (LRS \rightarrow HRS) voltage pulses. As confirmed by figure 7(a), the cell could sustain 210 switching cycles, maintaining a mean ON/OFF resistance ratio of 113 and a standard deviation $\sigma_{Rm} = 59$. In comparison to the LRS, the HRS displayed greater cycle-to-cycle

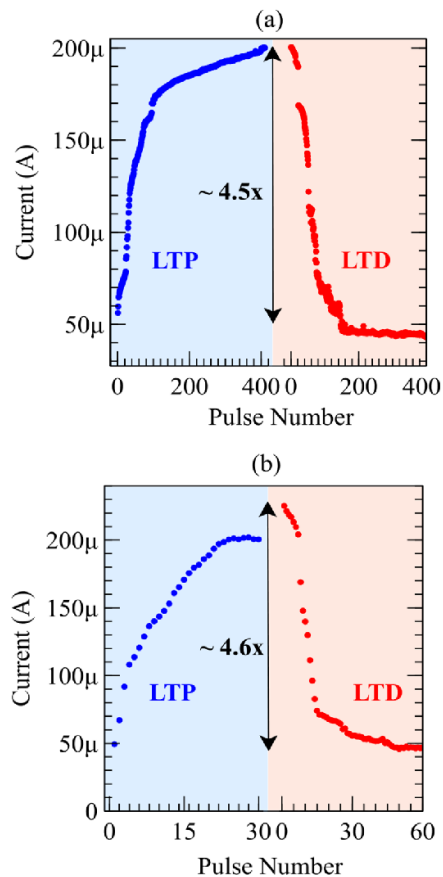


Figure 6. Gradual conductance switching i.e. long-term potentiation (LTP) and long-term depression (LTD) characteristics of the Ag–H₂O–Au LR switch. These results were achieved using +0.2 V set and –0.2 V reset pulse trains with 200 ms (in (a)) and 400 ms (in (b)) pulse widths.

variance (see figure 7(b)). This could be attributed to the following reasons: (a) limited accuracy of low current measurements using the Gamry potentiostat, (b) lack of precise control over the size of Ag filament erased, and (c) variations in the concentration of excess Ag⁺ ions in water. The last reason is particularly important considering that water-soluble Ag⁺ ions are released during each of the forming, set, and reset operations. As seen from figure 7, the ON/OFF resistance margin ($R_{\text{off}}/R_{\text{on}}$) decreased over the last ten cycles, culminating in a stuck-at-LRS condition in the 211th switching cycle. The apparent pre-failure HRS drift is suggestive of the incomplete dissolution of the previously deposited Ag filamentary material, which may be attributed to the build-up of excessive Ag⁺ ions in water [40, 47]. Although *in-situ* optical microscopy provides evidence of excessive Ag⁺ ion dissolution during the forming step, additional experiments monitoring the water-gap conductances are necessary to confirm this hypothesis. Overall, the Ag–H₂O–Au LR switches demonstrated better endurance compared with the recent demonstration of AgNO₃-based synapses [40]. Minimizing the cycle-to-cycle drift in HRS and matching up to the endurance of CMOS-based SR switches requires refining the programming framework. For instance, utilizing a current-limiting resistor

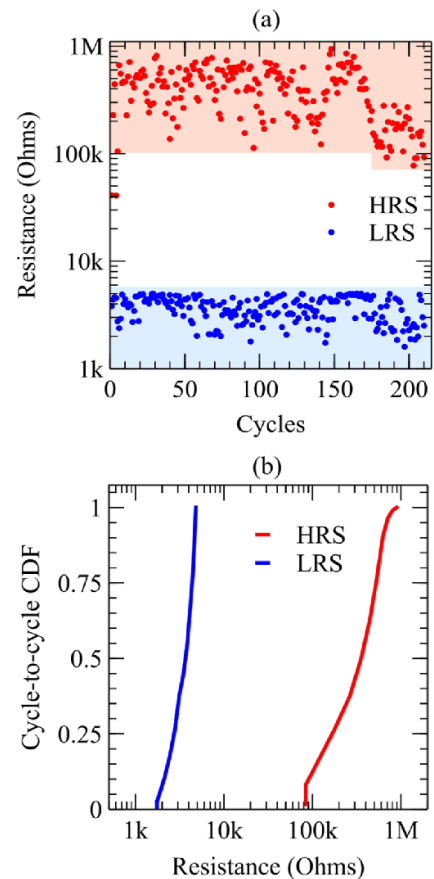


Figure 7. (a) Endurance of the Ag–H₂O–Au LR switch to repeated switching via the application of ± 0.2 V set (+) and reset (–) pulse trains and (b) the statistical spread of the measured LRS (blue) and HRS (red) resistances across all cycles.

in series with the Ag–H₂O–Au LR switch and enforcing a compliance voltage during the reset process would provide better control over the filament morphology and dissolution characteristics. In the context of improving device endurance, it is useful to note that unlike solid-state synapses, the Ag–H₂O–Au cell is amenable to physical resets, that is, in the event of device failure, the Ag link bridging the Ag and Au electrodes can be disintegrated by simply flowing water through the cross-point. As shown later in this section, this mechanism can be leveraged to extend device lifetimes beyond the onset of hard faults.

The non-volatility of synaptic conductances enables long-term memory and low power operation. Figure 5 confirmed this property in Ag–H₂O–Au LR switches, albeit over shorter time scales (sweep rate = 25 mV s^{–1}). As mentioned previously, water is a high diffusivity medium for Ag⁺ ions, and it encourages volatility of the programmed LRS conductances. In the absence of external power, a competition between the surface and volumetric energies of the high aspect ratio Ag link coupled with the enhanced diffusivity of Ag atoms in water promotes mechanical instabilities, such as the Rayleigh–Plateau instability, that naturally drive the cell toward the HRS [46, 48]; as a result, the temporal stability of the LRS is called into question. To fully characterize its retention

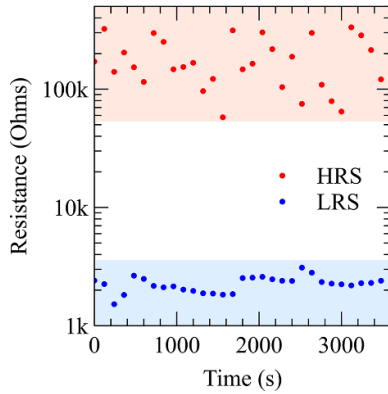


Figure 8. State retention characteristics of a representative Ag–H₂O–Au switch whose HRS and LRS was programmed using ± 0.2 V/1 s set (+) and reset (–) pulse trains.

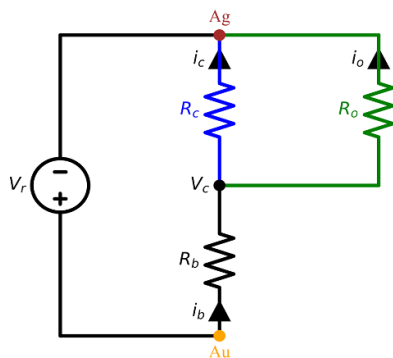


Figure 9. Simplified circuit model of the Ag–H₂O–Au LR switch highlighting the influence of LRS conductance on the magnitude of reset voltage. Here, V_r is the applied reset voltage, R_b is the resistance of the part of the filament that is not erased significantly during resets, R_c is the resistance of the filamentary segment that undergoes erasure and facilitates the LRS-to-HRS transition, and R_o represents the electrochemical resistance to Ag oxidation.

characteristics, the Ag–H₂O–Au switch was programmed to HRS and LRS (one at a time), and these states were monitored every two minutes over a total duration of two hours. Figure 8 shows the 1 h non-volatility of a representative Ag–H₂O–Au LR switch. At the end of an hour, the LRS degraded abruptly, thereby transforming the cell to HRS. The large 2- minute delays between consecutive reading pulses—deliberately chosen to minimize any influence of the read operation on the LRS stability—prevented the LRS conductance degradation from being resolved accurately in time. However, the typical exponential-like drop in LRS conductance at the end of the retention window was observed in other tests (results not included here) with the Ag–H₂O–Au switch [48, 49]. Note that the limited current resolution of the Gamry potentiostat (during the 50 mV/50 ms read operation) was chiefly responsible for the recorded variance in the HRS conductance.

Compared with the device in figure 8, which displayed a mean LRS resistance of 2.3 kΩ over 60 min, those with thicker filaments i.e. mean LRS resistance of 1.2 kΩ demonstrated higher retentivity ~ 120 min (results not shown here). However, erasing thicker filaments using low reset voltages i.e. -0.2 V/1 s proved to be a challenge and it typically

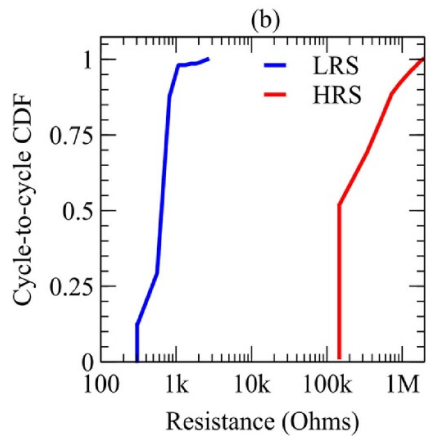
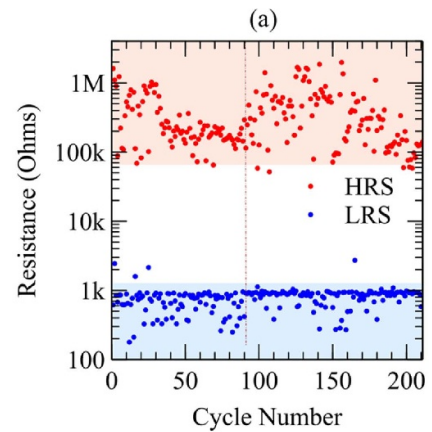


Figure 10. (a) Endurance of the Ag–H₂O–Au LR switch to repeated switching via the application of ± 2 V set (+) and reset (–) pulses. The dashed-dotted line denotes the instance when the water-gap was refreshed, and the device was ‘re-formed’. (b) The statistical spread of the measured LRS (blue) and HRS (red) resistances across all cycles.

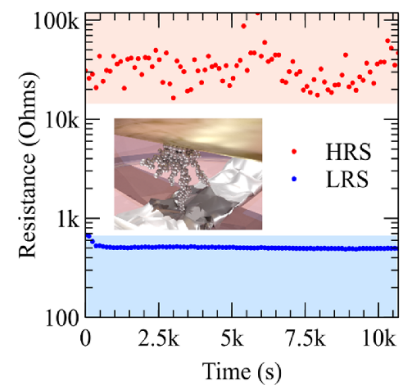


Figure 11. Non-volatility of a representative Ag–H₂O–Au LR switch. Here, the LRS was programmed using $+2$ V/1 s instead of $+0.2$ V/1 s set pulse trains and this promoted the growth of thicker filaments (see the middle inset).

resulted in permanent stuck-at-LRS failures. Achieving both high retention times and good reset reliability required (a) programming the device to highly conductive LRS and (b) utilizing higher reset voltages (-2 V/1 s). Figure 9 uncovers the direct relationship between the LRS conductance and the required reset voltage through a simplified circuit model of

Table 1. Comparative summary of this work vis-à-vis prior demonstrations of liquid-based resistive switches.

Work	Crossbar geometry	Electrode spacing	Switch medium	ON/OFF ratio	Set reset voltages	Endurance (# cycles)	Retention time	Analog switching
This work	Yes	40 μm	DI water	~ 600	± 0.2 V analog or ± 2 V digital	210	>3 h	Yes
Guo <i>et al</i> [39]	No	3 μm	DI water	~ 200	-0.3 V 0.4 V	2	N/A	N/A
Han <i>et al</i> [43]	No	6 μm	CuSO_4	~ 100	-0.1 V 0.4 V	500	N/A	N/A
Kim <i>et al</i> [40]	No	12 mm	AgNO_3	~ 5	-0.04 V 0.1 V	100	0.3 h	Yes
Sun <i>et al</i> [41]	No	N/A	KCl	~ 100	3 V -3.5 V	5	N/A	N/A
Hassan <i>et al</i> [42]	No	N/A	Water	~ 2.6	2.8 V -2.8 V	100	N/A	N/A

the Ag–H₂O–Au LR switch. Here, V_r is the amplitude of the reset pulse, R_b is the effective resistance of the highly conductive regions of the Ag link that do not participate directly in the resistive switching events, R_c is the effective electrical resistance of the highly resistive regions of the Ag filament that undergo growth (erasure) when subjected to set (reset) pulses, and R_o represents the charge transfer resistance to the oxidation of the resistive regions of the Ag link [50, 51]. Note that during the reset process the current i_o facilitates an increase in R_c by instigating the electrochemical oxidization and dissolution processes. From figure 9, the potential $\Delta V_{ox} = V_r - V_c$ across R_c can be calculated as:

$$\Delta V_{ox} = V_r \left(1 + R_b \left(\frac{1}{R_o} + \frac{1}{R_c} \right) \right)^{-1}. \quad (1)$$

To accelerate filament dissolution, ΔV_{ox} must be maximized using large values of V_r and R_c such that $R_c \gg R_b$. For Ag–H₂O–Au switches featuring high aspect ratio Ag links and large LRS conductances, the ratio R_c/R_b is relatively low, and hence achieving a sufficiently large ΔV_{ox} across R_c necessarily demands larger V_r . This explains why -2 V/1 s pulses proved to be more reliable in resetting Ag–H₂O–Au switches with LRS resistances less than 2 k Ω . However, using asymmetric set (0.2 V/1 s) and reset (-2 V/1 s) programming scheme frequently led to set failures, presumably because the gaps created by high-voltage erasures were too large for low voltage set pulses to bridge. This prompted the utilization of a symmetric $+2$ V/1 s set and -2 V/1 s reset pulse scheme which enabled quicker LRS \rightarrow HRS and HRS \rightarrow LRS transitions and higher ON/OFF current margins at the expense of analog operability. The suitability of this programming scheme for digital mode operation of Ag–H₂O–Au LR switches is confirmed by figure 10(a), which shows how these switches could sustain over 200 switching cycles while maintaining a very high ON/OFF resistance margin (mean) of ~ 600 . Figure 10(b) describes the spread of LRS and HRS resistances. In addition to describing its cyclability, figure 10(a) also highlights the amenability of Ag–H₂O–Au switches to fluidic resets. For example, between cycles 90 and 91 (dashed vertical line in figure 10(a)), the water inside the polyimide well (see figure 2) was substituted with a fresh droplet of deionized water. This water exchange destroyed the existing Ag link, requiring the Ag–H₂O–Au switch to be re-formed using $+2$ V DC before continuing further with the endurance test. However, as seen from figures 10(a) and (b), despite physically breaking and

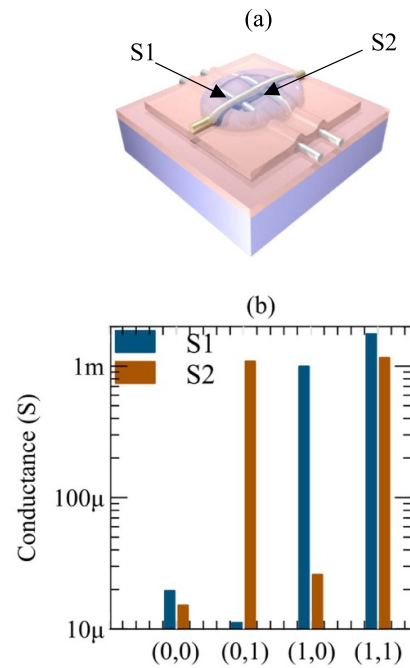


Figure 12. Programmability of a 2×1 Ag–H₂O–Au LR switch crossbar array. (a) Schematic illustration of the array. The two switches S1 and S2 are located at the crosspoints of overlapping Ag (bottom) and Au (top) wires. (b) Conductances of S1 and S2 measured after programming the array to each of the following states $(S1, S2) = \{(0,0), (0,1), (1,0), (1,1)\}$. Note that ‘0’ and ‘1’ denote HRS and LRS respectively.

reforming the Ag link, the Ag–H₂O–Au synapse displayed remarkable consistency in its LRS and HRS conductances. Also, thanks to the highly conductive LRS, the Ag–H₂O–Au LR switch maintained both HRS and LRS for at least 3 h (see figure 11).

To evaluate the prospect of building larger LR switch arrays, two Ag wires were overlapped over a single orthogonally oriented Au wire, producing the 2×1 crossbar sketched in figure 12(a). Switches 1 and 2, denoted as S1 and S2 respectively, were individually programmed to their respective LRS and HRS using ± 2 V/1 s pulse trains. After each programming step, the conductances of S1 and S2 were ascertained using 50 mV/50 ms read pulses. Figure 12(b) presents the measured conductances for each of the four programmed states $(S1, S2)$ of the 2×1 Ag–H₂O–Au array viz. (0,0), (0,1), (1,0), (1,1).

Note that ‘0’ and ‘1’ refer to the low conductance HRS and the high conductance LRS, respectively. This preliminary demonstration highlights the potential of building LR digital synapse networks using Ag–H₂O–Au crossbar switch arrays.

As summarized in table 1 above, the vertically oriented Ag–H₂O–Au LR switch crossbars demonstrated in this paper overcome some of the shortcomings associated with previous implementations of liquid-based switches.

4. Conclusion

This paper showed how a relatively high ion mobility medium, such as water, can be harnessed to build Ag–H₂O–Au long-range switches that are capable of interconnecting neurons as far apart as 40 μm. These electrochemical switches require low forming voltages to grow high aspect ratio Ag links across large water-gaps. Post-forming, subsequent low (high) voltage analog (digital) switching could be localized to the more resistive regions of the Ag link backbone. In addition to demonstrating analog and digital switching across a large conductance range, the Ag–H₂O–Au LR switches displayed good endurance and state retention. Unlike solid-state switches whose thin-film active layers cannot be etched and redeposited post-fabrication, Ag–H₂O–Au switches are amenable to physical resets via direct water-exchange. The simple construction, neuromorphic functionality, and fault-tolerability of Ag–H₂O–Au switches make them particularly attractive for neuromorphic wetware implementations.

Data availability statement

The data that support the findings of this study are available upon reasonable request from the authors.

ORCID iDs

Akshay Ananthkrishnan  <https://orcid.org/0000-0002-2791-9514>

Mark G Allen  <https://orcid.org/0000-0003-3963-6359>

References

- [1] Honey C J, Sporns O, Cammoun L, Gigandet X, Thiran J P, Meuli R and Hagmann P 2009 Predicting human resting-state functional connectivity from structural connectivity *Proc. Natl Acad. Sci. USA* **106** 2035–40
- [2] Park C, Kim S Y, Kim Y H and Kim K 2008 Comparison of the small-world topology between anatomical and functional connectivity in the human brain *Physica A* **387** 5958–62
- [3] Skudlarski P, Jagannathan K, Calhoun V D, Hampson M, Skudlarska B A and Pearlson G 2008 Measuring brain connectivity: diffusion tensor imaging validates resting state temporal correlations *Neuroimage* **43** 554–61
- [4] Zalesky A and Fornito A 2009 A DTI-derived measure of cortico-cortical connectivity *IEEE Trans. Med. Imaging* **28** 1023–36
- [5] Barbey A K 2018 Network neuroscience theory of human intelligence *Trends Cogn. Sci.* **22** 8–20
- [6] Bullmore E T and Bassett D S 2011 Brain graphs: graphical models of the human brain connectome *Annu. Rev. Clin. Psychol.* **7** 113–40
- [7] Leong A T L, Chan R W, Gao P P, Chan Y S, Tsia K K, Yung W H and Wu E X 2016 Long-range projections coordinate distributed brain-wide neural activity with a specific spatiotemporal profile *Proc. Natl Acad. Sci. USA* **113** E8306–15
- [8] Kutchko K M and Fröhlich F 2013 Emergence of metastable state dynamics in interconnected cortical networks with propagation delays *PLoS Comput. Biol.* **9** e1003304
- [9] Barttfeld P, Wicker B, Cukier S, Navarta S, Lew S and Sigman M 2011 A big-world network in ASD: dynamical connectivity analysis reflects a deficit in long-range connections and an excess of short-range connections *Neuropsychologia* **49** 254–63
- [10] Stepanyants A, Martinez L M, Ferecskó A S and Kisvárdy Z F 2009 The fractions of short- and long-range connections in the visual cortex *Proc. Natl Acad. Sci. USA* **106** 3555–60
- [11] Horvát S, Gămănuț R, Ercsey-Ravasz M, Magrou L, Gămănuț B, Van Essen D C, Burkhalter A, Knoblauch K, Toroczkai Z and Kennedy H 2016 Spatial embedding and wiring cost constrain the functional layout of the cortical network of rodents and primates *PLoS Biol.* **14** e1002512
- [12] Betzel R F and Bassett D S 2018 Specificity and robustness of long-distance connections in weighted, interareal connectomes *Proc. Natl Acad. Sci. USA* **115** E4880–9
- [13] Stehberg J, Stehberg J, Dang P T and Frostig R D 2014 Unimodal primary sensory cortices are directly connected by long-range horizontal projections in the rat sensory cortex *Front. Neuroanat.* **8** 93
- [14] Tang J et al 2019 Bridging biological and artificial neural networks with emerging neuromorphic devices: fundamentals, progress, and challenges *Adv. Mater.* **31** 1902761
- [15] Zhu J, Zhang T, Yang Y and Huang R 2020 A comprehensive review on emerging artificial neuromorphic devices *Appl. Phys. Rev.* **7** 011312
- [16] Strukov D B, Snider G S, Stewart D R and Williams R S 2008 The missing memristor found *Nature* **453** 80–3
- [17] Liu L et al 2020 Designing high-performance storage in HfO₂/BiFeO₃ memristor for artificial synapse applications *Adv. Electron. Mater.* **6** 1901012
- [18] Kim S, Choi S, Lee J and Lu W D 2014 Tuning resistive switching characteristics of tantalum oxide memristors through Si doping *ACS Nano* **8** 10262–9
- [19] Kumar S, Strachan J P and Williams R S 2017 Chaotic dynamics in nanoscale NbO₂ Mott memristors for analogue computing *Nature* **548** 318–21
- [20] Ani M H, Helmi F, Herman S H and Noh S 2018 Resistive switching of Cu/Cu₂O junction fabricated using simple thermal oxidation at 423 K for memristor application *IOP Conf. Series: Materials Science and Engineering* vol 290 p 012088
- [21] Adam G C, Hoskins B D, Prezioso M, Merrih-Bayat F, Chakrabarti B and Strukov D B 2017 3-D memristor crossbars for analog and neuromorphic computing applications *IEEE Trans. Electron Devices* **64** 312–8
- [22] Prezioso M, Merrih-Bayat F, Hoskins B D, Adam G C, Likharev K K and Strukov D B 2015 Training and operation of an integrated neuromorphic network based on metal-oxide memristors *Nature* **521** 61–4
- [23] Merrih-Bayat F, Guo X, Klachko M, Prezioso M, Likharev K K and Strukov D B 2018 High-performance mixed-signal neurocomputing with nanoscale floating-gate memory cell arrays *IEEE Trans. Neural Networks Learn. Syst.* **29** 4782–90
- [24] Alibart F, Zamanidoost E and Strukov D B 2013 Pattern classification by memristive crossbar circuits using *ex situ* and *in situ* training *Nat. Commun.* **4** 2072

- [25] Alibart F, Gao L, Hoskins B D and Strukov D B 2012 High precision tuning of state for memristive devices by adaptable variation-tolerant algorithm *Nanotechnology* **23** 075201
- [26] Li Y, Wang Z, Midya R, Xia Q and Joshua Yang J 2018 Review of memristor devices in neuromorphic computing: materials sciences and device challenges *J. Phys. D: Appl. Phys.* **51** 503002
- [27] Hu M, Strachan J P, Li Z and Williams S R 2016 Dot-product engine as computing memory to accelerate machine learning algorithms *Proc.—Int. Symp. Quality Electronic Design, ISQED (May 2016)* (IEEE Computer Society) pp 374–9
- [28] Lin P *et al* 2020 Three-dimensional memristor circuits as complex neural networks *Nat. Electron.* **3** 225–32
- [29] Truong S N, Ham S J and Min K S 2014 Neuromorphic crossbar circuit with nanoscale filamentary-switching binary memristors for speech recognition *Nanoscale Res. Lett.* **9** 629
- [30] Ananthkrishnan A and Allen M G 2020 All-passive hardware implementation of multilayer perceptron classifiers *IEEE Trans. Neural Networks Learn. Syst.* 1–10
- [31] Sokolov A S, Abbas H, Abbas Y and Choi C 2021 Towards engineering in memristors for emerging memory and neuromorphic computing: a review *J. Semicond.* **42** 013101
- [32] Amer S, Hasan M S and Rose G S 2018 Analysis and modeling of electroforming in transition metal oxide-based memristors and its impact on crossbar array density *IEEE Electron Device Lett.* **39** 19–22
- [33] Stathopoulos S, Khiat A, Trapatseli M, Cortese S, Serb A, Valov I and Prodromakis T 2017 Multibit memory operation of metal-oxide Bi-layer memristors *Sci. Rep.* **7** 17532
- [34] He W, Sun H, Zhou Y, Lu K, Xue K and Miao X 2017 Customized binary and multi-level HfO_{2-x}-based memristors tuned by oxidation conditions *Sci. Rep.* **7** 10070
- [35] Pan F, Yin S and Subramanian V 2011 A comprehensive simulation study on metal conducting filament formation in resistive switching memories *2011 3rd IEEE Int. Memory Workshop, IMW 2011* pp 1–4
- [36] Ling H, Koutsouras D A, Kazemzadeh S, Van De Burgt Y, Yan F and Gkoupidenis P 2020 Electrolyte-gated transistors for synaptic electronics, neuromorphic computing, and adaptable biointerfacing *Appl. Phys. Rev.* **7** 011307
- [37] Cramer T, Campana A, Leonardi F, Casalini S, Kyndiah A, Murgia M and Biscarini F 2013 Water-gated organic field effect transistors-opportunities for biochemical sensing and extracellular signal transduction *J. Mater. Chem. B* **1** 3728–41
- [38] Koo H J, So J H, Dickey M D and Velev O D 2011 Towards all-soft matter circuits: prototypes of quasi-liquid devices with memristor characteristics *Adv. Mater.* **23** 3559–64
- [39] Guo X, Schindler C, Menzel S and Waser R 2007 Understanding the switching-off mechanism in Ag+ migration based resistively switching model systems *Appl. Phys. Lett.* **91** 133513
- [40] Kim D and Lee J S 2019 Liquid-based memory and artificial synapse *Nanoscale* **11** 9726–32
- [41] Sun G, Slouka Z and Chang H C 2015 Fluidic-based ion memristors and ionic latches *Small* **11** 5206–13
- [42] Hassan G, Bae J, Khan M U and Ali S 2019 Resistive switching device based on water and zinc oxide heterojunction for soft memory applications *Mater. Sci. Eng. B* **246** 1–6
- [43] Han J H, Muralidhar R, Waser R and Bazant M Z 2016 Resistive switching in aqueous nanopores by shock electrodeposition *Electrochim. Acta* **222** 370–5
- [44] You B K, Kim J M, Joe D J, Yang K, Shin Y, Jung Y S and Lee K J 2016 Reliable memristive switching memory devices enabled by densely packed silver nanocone arrays as electric-field concentrators *ACS Nano* **10** 9478–88
- [45] Zhao M *et al* 2019 Characterizing endurance degradation of incremental switching in analog RRAM for neuromorphic systems *Technical Digest—Int. Electron Devices Meeting, IEDM (December 2018)* (Institute of Electrical and Electronics Engineers Inc.) p 20.2.1–4
- [46] Hsiung C P, Liao H W, Gan J Y, Wu T B, Hwang J C, Chen F and Tsai M J 2010 Formation and instability of silver nanofilament in Ag-based programmable metallization cells *ACS Nano* **4** 5414–20
- [47] Schindler C, Thermadam S C P, Waser R and Kozicki M N 2007 Bipolar and unipolar resistive switching in Cu-doped SiO₂ *IEEE Trans. Electron Devices* **54** 2762–8
- [48] La Barbera S, Vuillaume D and Alibart F 2015 Filamentary switching: synaptic plasticity through device volatility *ACS Nano* **9** 941–9
- [49] Zhao Y, Huang P, Zhou Z, Liu C, Qin S, Liu L, Liu X, Wong H S P and Kang J 2019 A physics-based compact model for CBRAM retention behaviors based on atom transport dynamics and percolation theory *IEEE Electron Device Lett.* **40** 647–50
- [50] Shen W *et al* 2018 Microfabricated intracortical extracellular matrix-microelectrodes for improving neural interfaces *Microsyst. Nanoeng.* **4** 30
- [51] Vitale F *et al* 2018 Biomimetic extracellular matrix coatings improve the chronic biocompatibility of microfabricated subdural microelectrode arrays *PLoS One* **13** e0206137